

## Induced ferromagnetism and metal-insulator transition due to a charge transfer effect in silver nanoparticle decorated MoS<sub>2</sub>

Shekhar Bag,<sup>1</sup> Shatabda Bhattacharya,<sup>1</sup> Diptiman Dinda,<sup>1</sup> M. V. Jyothirmai,<sup>2</sup> Ranjit Thapa,<sup>2</sup> and Shyamal K. Saha<sup>1,\*</sup>

<sup>1</sup>*Department of Materials Science, Indian Association for the Cultivation of Science, Jadavpur, Kolkata 700032, India*

<sup>2</sup>*SRM Research Institute and Department of Physics and Nanotechnology, SRM Institute of Science and Technology, Kattankulathur-603203, Tamil Nadu, India*



(Received 10 October 2017; revised manuscript received 28 June 2018; published 18 July 2018)

MoS<sub>2</sub> sheets are decorated by silver nanoparticles of size 10–12 nm. Localized holes are generated in Ag 4*d* levels carrying a magnetic moment due to the charge transfer effect at the interface and formation of Ag-S bonds. Temperature-dependent charge transport shows a metal-insulator (M-I) transition; the metallic phase is supported by the transition from negative to positive magnetoresistance and enhanced polarizability near the M-I transition. Observed ferromagnetism arises due to dominant coupling among the spins of localized holes in Ag nanoparticles at lower temperature. Density functional theory calculation is carried out to establish the charge transfer effect. The amount of charge transferred from Ag to MoS<sub>2</sub> is evaluated from Bader charge analysis and the temperature effect is verified by a Nosé thermostat with the *NVT* ensemble method.

DOI: [10.1103/PhysRevB.98.014109](https://doi.org/10.1103/PhysRevB.98.014109)

### I. INTRODUCTION

Since the discovery of graphene in 2004, research activities on two-dimensional (2D) materials have accelerated remarkably, especially during the last decade [1–5]. Considering superior semiconducting properties compared to graphene, metal dichalcogenide, viz., MoS<sub>2</sub> in particular, shows promising applications in various areas like electronic devices [6], optoelectronics [7,8], spintronics [9,10], electrocatalysts [11,12], photocatalysts [13], and hydrogen evolution [14]. In addition to superior intrinsic properties, doping or functionalization processes are the elegant approaches used to tune the existing properties or the introduction of new properties in MoS<sub>2</sub> [15–19]. Because of the highly reactive defect states (S or Mo vacancies), the MoS<sub>2</sub> surface is prone to attaching other atoms/molecules to decorate the surface for generating new properties. The even, clean MoS<sub>2</sub> surface is also moderately reactive due to lone pair electrons of S atoms developing nanostructures of metals, semiconductors, or molecules on it.

During the past few years interesting magnetic properties have been developed in thiol-capped noble metal nanostructures due to strong interaction of noble metals such as gold (Au) and silver (Ag) with thiol as a result of charge transfer between them [20–22]. Permanent magnetism, magnetic anisotropy, and a ferromagnetic hysteresis loop with coercivity of 860 Oe at 5 K were reported in thiol-capped gold nanoparticles [20]. Subsequently, similar results of ferromagnetic ordering associated with blocked, highly anisotropic localized magnetic moments at the surface of the Ag nanoparticle were also reported due to the spins of 4*d* localized holes generated through Ag-S bonds [21]. Although some efforts to develop magnetism in noble metals using strong interaction of thiol with Au, Ag, etc., have already been made, the approach has

not yet been sufficiently explored to introduce magnetism in Ag nanoparticles decorated on the MoS<sub>2</sub> surface via strong interaction between Ag and S.

In the present work, we have exploited this strong interaction between Ag and thiol to tune the material properties of MoS<sub>2</sub> by growing Ag nanoclusters on the MoS<sub>2</sub> surface. The insulator-to-metal transition and ferromagnetic ordering in the low-temperature region are observed in this Ag nanoparticle decorated MoS<sub>2</sub>. The metallic phase is also supported by the enhanced polarizability resulting in high capacitance and transition from negative to positive magnetoresistance near the metal-to-insulator (M-I) transition. All these results of M-I transition and observed ferromagnetic ordering at low temperature are explained on the basis of charge transfer from silver to MoS<sub>2</sub> introducing additional impurity levels at the Fermi energy and enhanced magnetic coupling among the spins of localized holes in Ag nanoparticles, respectively, at lower temperature.

### II. SYNTHESIS AND STRUCTURAL CHARACTERIZATION

We have synthesized silver nanoparticle decorated molybdenum disulfide sheets with two different concentrations of silver (Ag). In the first step, we synthesized cetyltrimethylammonium bromide (CTAB) assisted MoS<sub>2</sub> sheets. For this, we took 100 mg of Mo salt, i.e., hexa ammonium heptamolybdate tetrahydrate, along with 100 mg of CTAB in 30 ml of double distilled (dd) water and stirred for 30 min. Then, 200 mg of thiourea was added to the solution and stirred for another 30 mins. After that, the clear solution was transferred into a 50-ml Teflon-lined stainless-steel autoclave and heated at 200 °C for 30 h. The resultant product was washed with water and ethanol for several times to remove all unreacted molecules/ions. Finally, it was dried at 60 °C under vacuum to get powdered MoS<sub>2</sub> material. In the second step, we used that

\*cnsks@iacs.res.in

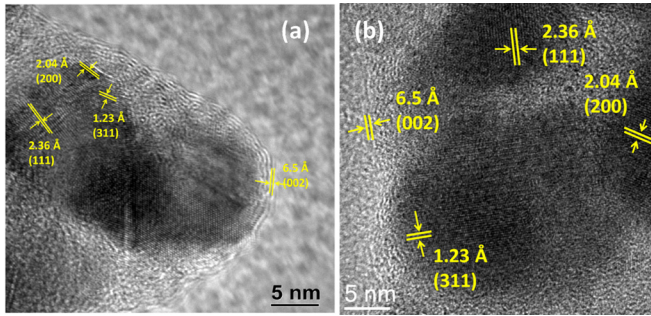


FIG. 1. TEM micrographs of as-synthesized MoS<sub>2</sub> sheets decorated by Ag nanoparticles. (a) High-resolution lattice image of sample S1. (b) High-resolution lattice image of sample S2. The lattice spacings of different planes are also shown in the high-resolution lattice images.

CTAB assisted MoS<sub>2</sub> material to decorate Ag nanoparticles over it. Firstly, 25 mg of MoS<sub>2</sub> was dissolved in 50 ml of dd water and stirred for 2 h to form a homogeneous dispersion. For good dispersion, again 100 mg of CTAB was added into the mixture and stirred for another 30 min. Then, 0.8 mM of aqueous AgNO<sub>3</sub> solution was added slowly to it with continuous stirring. After 30 min, 20 mM of NaBH<sub>4</sub> followed by 10 mM of ascorbic acid solutions were quickly injected into the mixture and stirred for another 2 h with mild heating at 70 °C. An immediate darkening of the solution was observed due to the formation of Ag nanoparticles over MoS<sub>2</sub>. The resultant product (S1) was then washed with dd water and ethanol for several times to remove all unreacted molecules. Finally, it was dried at 60 °C in a vacuum oven to get the powdered material. We have followed the same procedures to synthesize another batch of sample (S2) using 1.2 mM of AgNO<sub>3</sub> solution with the same concentration of MoS<sub>2</sub>.

### A. TEM microstructure analysis

Transmission electron microscopy (TEM) was carried out using a JEOL-2011 high-resolution transmission electron microscope to understand the morphology, size, and crystallinity of silver nanoclusters. Figures 1(a) and 1(b) show the TEM micrographs of silver nanoparticles decorated on MoS<sub>2</sub> nanosheets and their high-resolution lattice images for samples S1 and S2, respectively. The particle size is estimated as 10–12 nm. Both the figures reveal the microstructure of an as-synthesized MoS<sub>2</sub> nanosheet with interlayer separation of 6.5 Å corresponding to the (002) plane of layered-type MoS<sub>2</sub>. From the high-resolution lattice image, the silver nanoparticles are confirmed by measuring the lattice spacing of 2.36, 2.04, and 1.23 Å corresponding to the (111), (200), (311) planes of crystalline silver nanoparticle, respectively. To understand the growth of Ag nanoparticles on the MoS<sub>2</sub> surface we have done elemental mapping of the composite material as shown in Fig. 2. From the mapping figure it is clear that Ag nanoparticles are distributed throughout the MoS<sub>2</sub> surface. From this image, distribution of Ag over MoS<sub>2</sub> can be clearly visualized. To check the stoichiometric ratio and atomic percentage of the composite material we have performed energy dispersive x-ray (EDX) analysis of the composite material as given in Fig. 3(a).

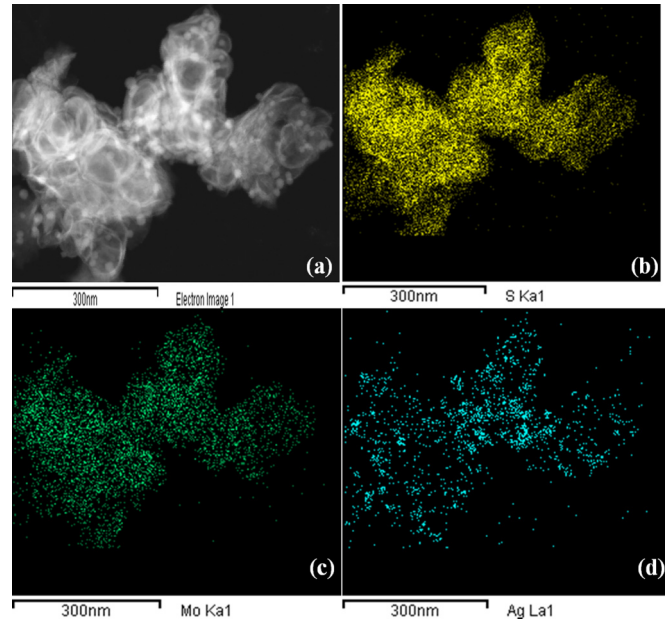


FIG. 2. Element mapping by transmission electron microscopy of a typical Ag@MoS<sub>2</sub> sample. (a) The portion of the composite where element mapping is performed. Mapping of individual element (b) sulfur (S), (c) molybdenum (Mo), (d) silver (Ag).

From this it is seen that the ratio of the atomic percentage of Mo and S is  $\sim 1:2$ ; i.e., good quality MoS<sub>2</sub> has been formed. The atomic percentage of Ag nanoparticles has also been obtained from it as given in Fig. 3(a).

### B. Analysis of residual doping of MoS<sub>2</sub>

We have carried out inductively coupled plasma optical emission spectrometry (ICP OES) analysis using PerkinElmer DV ICP OES to study the effect of residual doping of MoS<sub>2</sub>. We have prepared the sample for ICP OES measurement as follows:

The as-synthesized 2 mg of MoS<sub>2</sub> powder was put into 10 ml of 10% HNO<sub>3</sub> (Suprapur, Merck, 65%) solution. The acid solution mixed with MoS<sub>2</sub> is then ultrasonicated for 30 min in an ultrasonic bath. The concentration of MoS<sub>2</sub> in this solution is 0.2 mg/ml. Then, 0.1 ml of solution from the above ultrasonicated mixer is taken and diluted 100 times using 10 ml of 10% HNO<sub>3</sub> solution with it. The concentration of MoS<sub>2</sub> is 0.002 mg/ml. We have carried out ICP-OES measurement with the diluted solution containing 0.002 mg/ml of MoS<sub>2</sub>. We have also prepared another solution of the composite (Ag@MoS<sub>2</sub>) with a concentration of 0.002 mg/ml by the same procedure. The concentrations of the elements Mo and S in MoS<sub>2</sub> as obtained from ICP-OES analysis is shown in Table I. The concentrations of Ag, Mo, and S in the composite are also given in Table I. From the concentrations as obtained from the ICP-OES study we have calculated the percentages of the elements present as shown in the table. Therefore, the presence of residual dopant atoms/elements in MoS<sub>2</sub> as well as in the composite is very low in comparison to the actual concentrations of Mo and S in MoS<sub>2</sub> and Ag, Mo, and S in the composite material. From the ICP-OES analysis it is found that MoS<sub>2</sub> in the present composite contains mostly

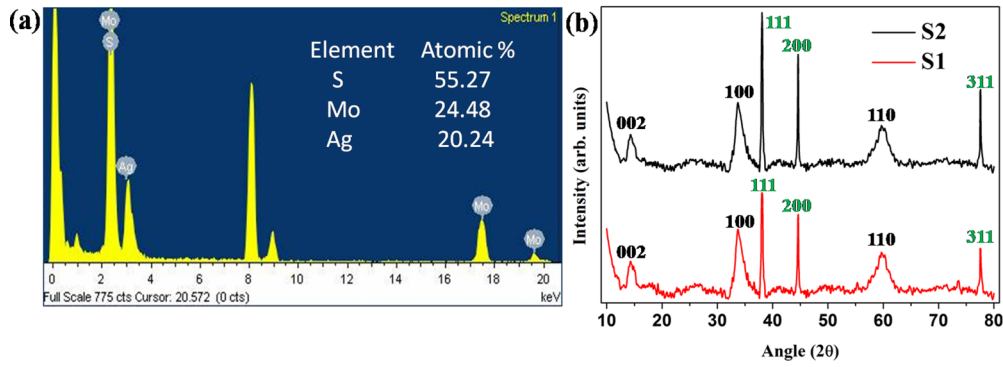


FIG. 3. (a) Energy dispersive x-ray spectroscopy (EDS) study to determine elements present in the sample. (b) The XRD patterns of samples S1 and S2 show peaks corresponding to Ag (green) and MoS<sub>2</sub> (black).

Mo and S and maintains nearly a 1:2 stoichiometric ratio. The Ag percentage as obtained from the ICP-OES analysis is about 18.65%. Hence, the presence of residual dopant atoms/elements, if any, in MoS<sub>2</sub> has no effect on the observed results.

### C. XRD study

We have performed x-ray diffraction (XRD) measurements using an x-ray diffractometer (Rich. Seifert XRD 3000P with an x-ray generator, Cu, 10 kV, 10 mA, wavelength 1.5418 Å). Figure 3(b) shows the baseline corrected XRD patterns of samples S1 and S2. All the peaks are matched with JCPDS card no: 04-0783 for Ag and 24-0513 for the MoS<sub>2</sub> phase. From the XRD analysis it is seen that three peaks appear at 38.159°, 44.330°, and 77.552° corresponding to Ag (111), (200), and (311) planes (green), respectively. The peaks appearing at 14.2°, 33.1°, and 58.9° correspond to MoS<sub>2</sub> (002), (100), and (110) planes (black), respectively, as shown in Fig. 3(b). The intensities of the Ag peaks are reduced as the silver precursor concentration is reduced from S2 to S1.

### D. XPS analysis and verification of charge transfer

X-ray photoelectron spectroscopy (XPS) measurement has been carried out in an Omicron-0571 system. From Fig. 4(a) it has been observed that for the Ag decorated MoS<sub>2</sub> (Ag@MoS<sub>2</sub>) sample three peaks appear at 233.50, 397.38, and 415.68 eV corresponding to Mo 3*d*, Mo 3*p*<sub>3/2</sub>, and Mo 3*p*<sub>1/2</sub> orbitals, respectively. Ag 3*d* and S 2*p* orbital peaks have also been observed in an Ag@MoS<sub>2</sub> composite material XPS pattern. The XPS spectrum of bare Ag nanoparticles produced by the same procedure in the absence of MoS<sub>2</sub> nanosheets is shown in Fig. 4(b). We have also carried out XPS analysis of

TABLE I. The calculated percentages of elements from ICP-OES analysis.

Material	Ag (%)	Mo (%)	S (%)	Residue percentage (%)
MoS <sub>2</sub>	0	32.9	66.55	0.55
Ag@MoS <sub>2</sub>	18.65	26.5	54.4	0.45

as-synthesized pristine MoS<sub>2</sub> nanosheets without the presence of Ag nanoparticles as shown in Fig. 4(c). At 369.08 and 375.14 eV two peaks corresponding to Ag 3*d*<sub>5/2</sub> and 3*d*<sub>3/2</sub> orbitals appear as shown in a magnified XPS pattern of Fig. 5(a) for Ag@MoS<sub>2</sub>. Ag 3*d*<sub>5/2</sub> and 3*d*<sub>3/2</sub> peaks appear at 368.21 and 374.23 eV, respectively, as shown in the magnified XPS pattern of Fig. 5(b) for Ag nanoparticles. The magnified XPS pattern of the S 2*p* orbital in Fig. 5(c) shows that there are two peaks at 162.25 and 163.30 eV corresponding to S 2*p*<sub>3/2</sub> and S 2*p*<sub>1/2</sub> orbitals of the Ag@MoS<sub>2</sub> composite. In the magnified S 2*p* XPS pattern of pristine MoS<sub>2</sub> nanosheets, S 2*p*<sub>3/2</sub> and 2*p*<sub>1/2</sub> peaks appear at 163.06 and 164.11 eV, respectively, as shown in Fig. 5(d). To understand the charge transfer process at the interface of Ag and MoS<sub>2</sub> we have compared the binding energies of the S 2*p* orbital of pristine MoS<sub>2</sub> nanosheets and the Ag 3*d* orbital of bare Ag nanoparticles with that of the Ag@MoS<sub>2</sub> composite system. It has been observed that the binding energies of the Ag 3*d*<sub>5/2</sub> and Ag 3*d*<sub>3/2</sub> states increase by 0.86 and 0.89 eV, respectively; however, for S 2*p*<sub>3/2</sub> and S 2*p*<sub>1/2</sub> orbitals binding energies decrease by 0.81 and 0.83 eV, respectively, for the Ag@MoS<sub>2</sub> composite. Therefore, it is confirmed from XPS study that charge transfer occurs from Ag 3*d* to S 2*p* at the interface. The comparison of binding energy values of orbitals are given in Table II. Such type of charge transfer from Ag to S through the Ag-S bond is also reported in the literature [21]. Sometimes the shift in binding energy may be superimposed due to initial/final state effects. Generally, the final state effect is essential for size-dependent metal clusters placed on an insulating substrate and it refers to the relaxation (screening) effect that takes place after the photoemission process. The insulator being a poorly conducting substrate, this mechanism occurs on a longer time scale than the XPS measurement time [23]. This will be absent in a moderately conducting substrate like MoS<sub>2</sub>. The final state effect will be important for metallic substrates and can be excluded for semiconducting substrates [24]. Sometimes this effect is also formed due to the metal-oxygen bond. MoS<sub>2</sub> being a chalcogenide there is no formation of a metal-oxygen bond which would lead to the final state effect. Also the initial state effect may originate from interfacial chemical reactions and the presence of defects [25]. In our case because Ag is a noble metal we have not considered any interfacial change, and no presence of oxygen peaks is observed. Thus we have eliminated the presence of any state effect.

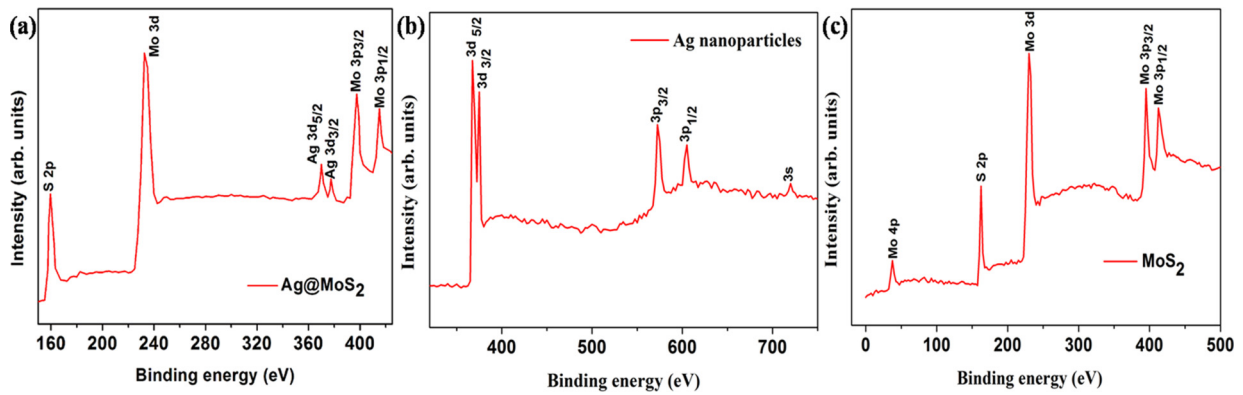


FIG. 4. Full-range XPS spectra of (a) Ag@MoS<sub>2</sub> composite, (b) Ag nanoparticles, (c) pristine MoS<sub>2</sub>.

### III. RESULTS AND DISCUSSION

#### A. Resistivity measurement as a function of temperature

We have performed a standard four-probe method for resistivity measurement using pellet samples of diameter 6 mm and thickness 1 mm. The pellets are made in a hydraulic press under 3 tons pressure. Conductive silver paste (Alfa Aesar) is used for contact electrodes. Resistivity measurement is carried out in a standard PPMS system with a closed cycle cryostat (Janis) having a cold head (Sumitomo). Current

and voltage are measured by a sourcemeter (Keithley 2601) and a nanovoltmeter (Keithley 2182A) with current-in-plane geometry. Data acquisition is done through a LABVIEW 8.5 interface. We have given a schematic diagram for measurement setup in Fig. 6(a). Figures 7(a) and 7(b) show the resistivity as a function of temperature (4–300 K) for the samples S1 and S2. It is seen that the resistivity initially increases exponentially with decreasing temperature and then decreases down to a certain temperature and finally increases again down to 4 K, the lowest measured temperature. From the temperature variation

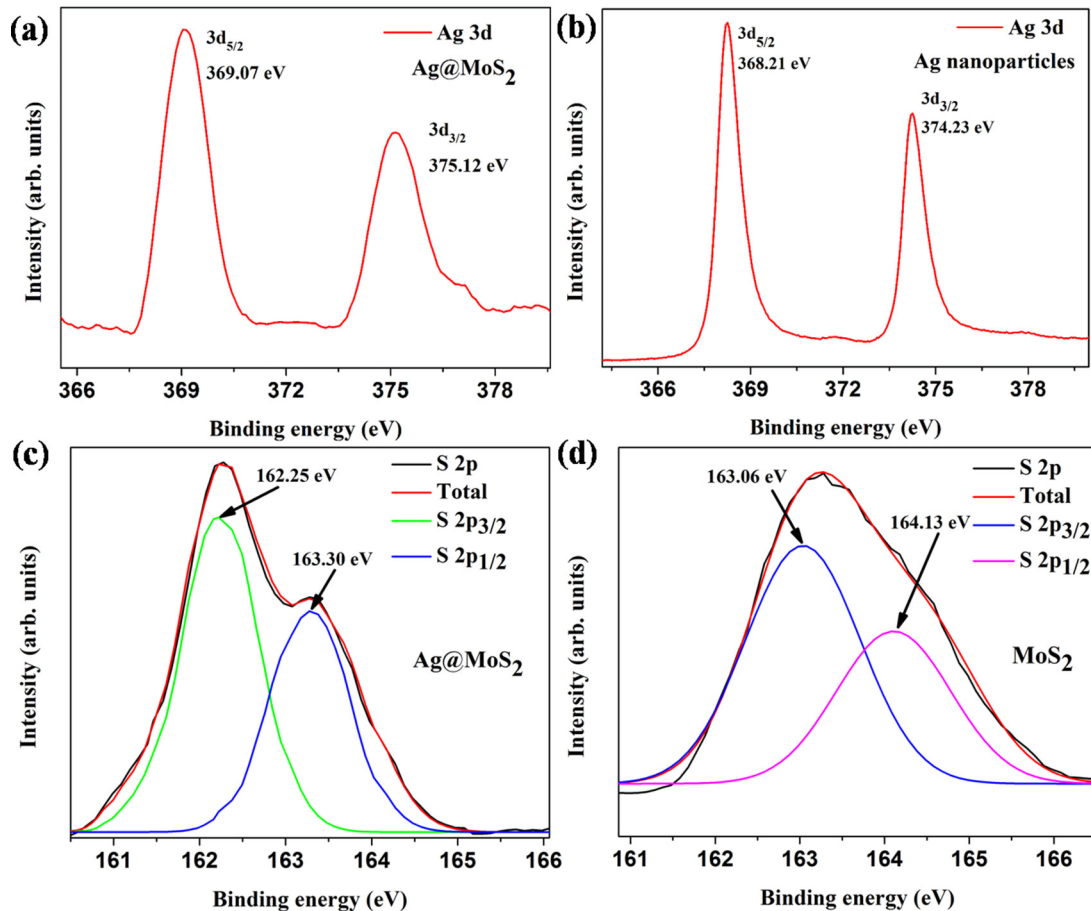


FIG. 5. Magnified XPS spectra of Ag 3d orbitals for (a) Ag@MoS<sub>2</sub> composite, (b) Ag nanoparticles and S 2p orbitals for (c) Ag@MoS<sub>2</sub> composite, (d) pristine MoS<sub>2</sub>.

TABLE II. Binding energy shift from XPS analysis.

Elements	Orbitals	Binding energy (eV) of Ag@MoS <sub>2</sub> composite	Binding energy (eV) of bare Ag nanoparticles	Shift in binding energy (eV)
Ag	3d <sub>5/2</sub>	369.07	368.21	0.86
	3d <sub>3/2</sub>	375.12	374.23	0.89
S			Binding energy (eV) of pristine MoS <sub>2</sub>	
	2p <sub>3/2</sub>	162.25	163.06	-0.81
	2p <sub>1/2</sub>	163.30	164.13	-0.83

of resistivity, it appears that the sample shows a complex behavior because of the presence of silver nanoclusters on the MoS<sub>2</sub> surface. The band structure of MoS<sub>2</sub> is modified significantly due to the charge transfer occurring between Ag and MoS<sub>2</sub> as obtained from XPS data. We have also carried out temperature-dependent resistivity measurement of pristine MoS<sub>2</sub> as shown in Fig. 7(c) and compared the resistivity of pristine MoS<sub>2</sub> with the resistivity of samples S1 and S2 as shown in Fig. 7(d). It is seen that the resistivity values of samples S1 and S2 are enhanced in comparison to pristine MoS<sub>2</sub> due to silver decoration.

To investigate this complex behavior of resistance we have taken the expression for resistivity as

$$\rho = \frac{1}{ne\mu}, \quad (1)$$

where  $n$  is the carrier concentration,  $e$  is the electronic charge, and  $\mu$  is the mobility.

We have taken the carrier concentration as [26]

$$n = n_0 \left[ 1 + n_1 \exp\left(-\frac{\phi}{k_B T}\right) \right], \quad (2)$$

where  $\phi$  is the activation energy in meV,  $k_B$  is the Boltzmann constant, and  $n_0$  is the carrier concentration at  $T \rightarrow 0$  K.

To understand this complex charge transport using a realistic model we have considered the mobility expression as

$$\frac{1}{\mu} = \frac{1}{\mu_0} + \frac{1}{\mu_{e-p}} + \frac{1}{\mu_L}, \quad (3)$$

where  $\mu_0$  is the temperature-independent contribution due to scattering of electrons with grain boundaries [26] and neutral impurities [27,28].  $\mu_{e-p}$  is the contribution to mobility due to electron-phonon scattering. However, the third term in the mobility expression has been included to incorporate the disorder-induced localized charge transport (Anderson-type localization) that occurs in the low-temperature region. At low temperature, both the effects of charge transfer from Ag to S and the disorder in the MoS<sub>2</sub> lattice arising due to the presence of Ag nanoclusters cause localization in the system. When the extent of disorder is sufficiently large to induce the Fermi energy to cross the mobility edge, i.e., to place the Fermi energy in the region of localized states, there is a transition from the metallic state to a nonmetallic state. This disorder-induced M-I transition is called the ‘‘Anderson transition.’’ As the disorder increases, the materials become more insulating, and the conductivity decreases more rapidly upon lowering temperature; i.e.,  $\rho$  increases. Therefore, to include this effect in the low-temperature region we have considered the charge transport in this region as dominated by that of the critical regime of metal-insulator (M-I) transition. In the critical regime, the resistivity follows the power-law behavior as given by [29]

$$\frac{1}{\mu_L} \propto \rho_L = \alpha T^{-\beta}, \quad (4)$$

where  $\alpha$  is a constant and  $\beta$  is an exponent giving rise to the degree of disorder or localization.

Considering electron-phonon scattering and mobility as a decreasing function with increasing temperature we have taken [30]

$$\frac{1}{\mu_{e-p}} = BT^k, \quad (5)$$

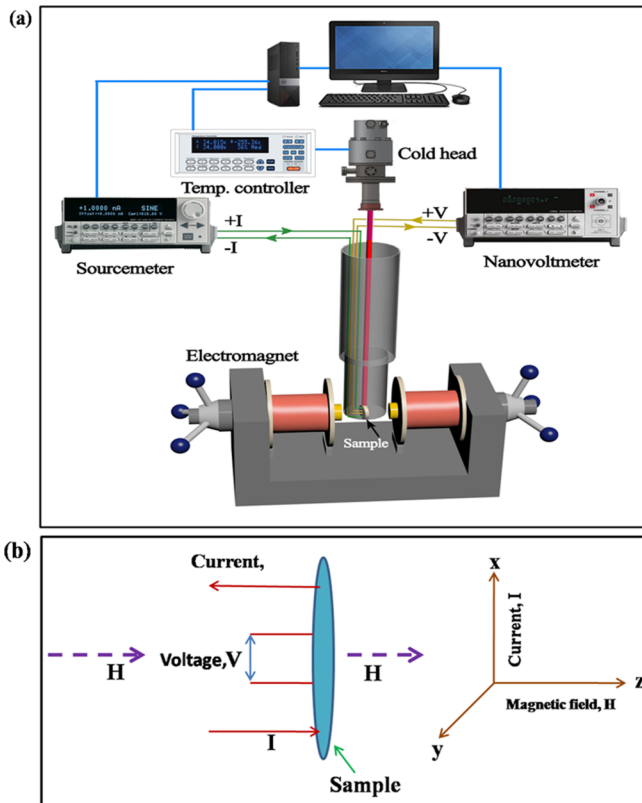


FIG. 6. Schematic diagram of experimental geometry for (a) resistivity measurement as a function of temperature, and (b) magnetoresistance measurement.

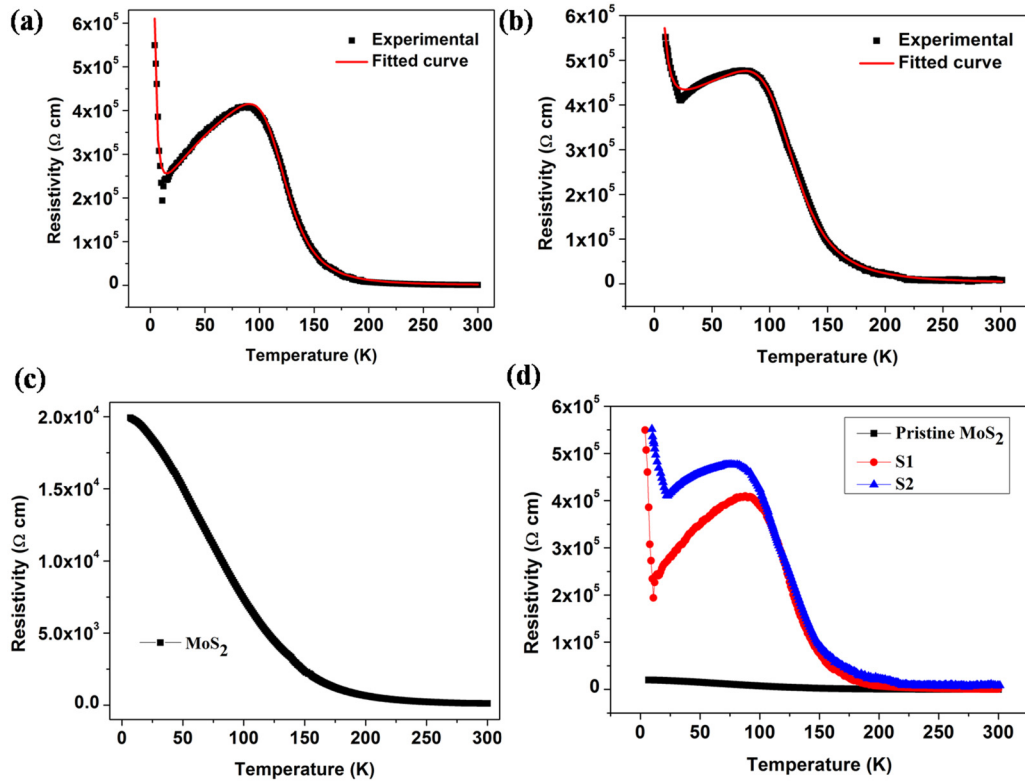


FIG. 7. Resistivity as a function of temperature for samples (a) S1 and (b) S2. The red lines represent the curves fitted with Eq. (4) and the points are the experimental data. (c) Temperature-dependent resistivity of pristine MoS<sub>2</sub> nanosheets. (d) Comparison of temperature-dependent resistivity of samples S1 and S2 with pristine MoS<sub>2</sub>.

where  $B$  is a constant and  $k$  is the exponent which measures the strength of temperature variation.

The charge transfer from Ag to MoS<sub>2</sub> through the interaction between Ag and S and its effect to low temperature rise in resistivity in terms of localized charged transport is incorporated by a factor  $\alpha T^{-\beta}$  in the mobility expression. This charge transfer from Ag to MoS<sub>2</sub> is due to overlapping of orbitals at the interface. The coupling is better at low temperature than at high temperature because at high temperature due to thermal fluctuation the overlapping will be less. The temperature-dependent charge transfer has been confirmed by theoretical DFT calculation also. From this study it is found that the integral value of valence electron of Ag reduces at lower temperature which means that charge is transferred more at lower temperature. The detail calculation is given later. Because of this induced extra charge as well as disorder created by Ag nanoclusters, MoS<sub>2</sub> lattice alters its band structure by generating localized levels near Fermi energy. It is also noted that the density of these localized levels increase with decreasing temperature.

Therefore considering temperature-independent mobility term as a constant  $A$  ( $\frac{1}{\mu_0} = A$ ) and substituting other mobility terms corresponding to electron-phonon interaction and the contribution due to disorder-induced charge transport in the critical regime of M-I transition, the final expression for mobility becomes

$$\frac{1}{\mu} = \frac{1}{\mu_0} + \frac{1}{\mu_{e-p}} + \frac{1}{\mu_L} = A + BT^k + \alpha T^{-\beta}. \quad (6)$$

Therefore, putting  $\frac{1}{\mu} = A + BT^k + \alpha T^{-\beta}$  and  $n = n_0[1 + n_1 \exp(-\frac{\phi}{k_B T})]$  in Eq. (1) we get

$$\rho = \frac{A + BT^k + \alpha T^{-\beta}}{en_0[1 + n_1 \exp(-\frac{\phi}{k_B T})]} = \frac{a(1 + bT^k) + \alpha T^{-\beta}}{en_0[1 + n_1 \exp(-\frac{\phi}{k_B T})]}, \quad (7)$$

where  $a = A$  and  $b = \frac{B}{A}$ .

The resistivity data shown in Figs. 7(a) and 7(b) are fitted using the expression given in Eq. (7) and it is seen that the experimental data are well fitted with the proposed model. The solid curve represents the complex behavior of resistivity as given in Eq. (7) whereas the data points are the experimental result. The most interesting result in the resistivity data is the metal-like behavior in the intermediate temperature region. Though crystalline MoS<sub>2</sub> behaves like an intrinsic semiconductor [31], however, the presence of silver nanoclusters on the MoS<sub>2</sub> surface modifies the band structure due to disorder created at the MoS<sub>2</sub> lattice and charge transfer from Ag to S through formation of Ag-S bonds [21]. In the proposed model of charge transport shown in Eq. (7), there are three functional forms of resistivity as a function of temperature. The denominator represents the activating process at the high-temperature limit; however, in the numerator the first term gives the metal-like [32] behavior in the intermediate temperature range. We have introduced the last term to incorporate the disorder-induced localized charge transport near the M-I transition for which resistance again

increases in the low-temperature region. The transition from metal-like behavior to insulating nature occurring here is due to enhanced transfer of charge which increases the density of localized states at low temperature, which in turn increases the degree of disorder in the system giving rise to disorder-induced localization, i.e., the Anderson transition. With a decrease in temperature, the charge transfer rate increases more which creates more localized levels. Thus with decreasing temperature, a metal-like behavior is observed due to a decrease in energy gap between the localized states. When the thermal energy of an electron exceeds the average energy gap between the localized states, the system behaves like a metal [33]; however, with further decrease in temperature, enhancement of localized levels dominates to initiate disorder-induced localization due to a greater number of localized charges transferred from Ag to MoS<sub>2</sub> at a lower temperature to increase the resistivity at the lowest-temperature region.

A metal-insulator transition can occur either by electron-electron interaction or by disorder, but the two localized electron phases are distinct. Mott transition usually occurs in an interacting electronic system in which electron-electron interaction (Coulomb repulsion) enhances the resistivity of the system going to very low temperature and the system behaves as a Mott insulator, whereas a true Anderson transition is obtained due to randomly oriented impurities or disorders. The metallic phase is obtained when neither disorder nor electron-electron interaction is too large. In this case as the charge transfer increases at very low temperature, it enhances the disorderedness of the system and hence localization is of the Anderson type. Introduction of Ag nanoclusters over the MoS<sub>2</sub> surface influences the degree of disorderedness of the system. Here disorder-induced localization is dominant, i.e., Anderson type.

To explain the temperature-dependent complex resistivity of the present silver decorated MoS<sub>2</sub> sample we have introduced in the mobility expression only the contribution due to disorder-induced charge transport in the critical regime of M-I transition. As a result, in the high-temperature region, electron-phonon scattering is the dominant contribution in the resistivity which shows activated-type transport. However, in the low-temperature region disorder-induced M-I transition plays an important role in controlling the overall resistivity of the sample. The values of the parameters as obtained by the fitting procedure using Eq. (7) are summarized in Table III.

TABLE III. Parameters obtained after fitting the  $R$ - $T$  curves with Eq. (7).

Parameters	S1		S2	
	Value	Standard error	Value	Standard error
$a$ ( $\Omega$ cm)	498.103	1.263	449.335	0.891
$b$ ( $K^{-1}$ )	158.185	0.429	478.027	0.949
$k$	0.3724	0.0434	0.1808	0.087
$\alpha$ ( $\Omega$ cm K)	11543.625	172.174	30269.273	22.336
$\beta$	1.8066	0.1996	1.5814	0.1169
$n_0$ ( $cm^{-3}$ )	$6.25 \times 10^{18}$	312.6789	$9.375 \times 10^{18}$	405.6652
$n_1$	12.378	0.07677	50.723	0.0868
$\phi$ (meV)	105	19.13	84	7.50

As mentioned above, the presence of silver nanoparticles on the MoS<sub>2</sub> surface produces some closely spaced localized levels with an energy gap between two levels as 105 meV for S1 and 84 meV for S2 near the conduction band [34]. In the high-temperature region, due to higher thermal energy, these localized electrons move to the conduction band to contribute in the conductivity. With decreasing temperature localized impurity levels due to charge transfer increase and at an intermediate temperature the resistivity shows metal-like behavior. At very low temperature, resistivity again increases due to disorder-induced charge transport because of the enhanced charge transfer from Ag to MoS<sub>2</sub> and the disorder created by Ag nanoclusters. The temperature dependence of localization is related through the charge transfer effect. With decreasing temperature, charge transfer increases, which in turn enhances the overall disorderedness of the system, i.e., localization. The effect of this is to increase the probability of scattering of electrons with the disorder potentials and hence decrease the conductance. As a result the system becomes more insulating at low temperature.

### B. Magnetotransport measurement

To understand the effect of magnetic field on charge transfer from Ag to MoS<sub>2</sub> at the interface and its interaction with the conduction electrons we have investigated magnetotransport over the temperature range from 6 to 300 K for sample S1 and from 10 to 300 K for sample S2 and magnetic field up to 2.0 T. We have measured magnetoresistance in a standard PPMS system (in four probe) as described schematically in Fig. 6(a). Device geometry was the current-in-plane method. From Fig. 6(a) it is seen that the sample is placed vertically inside the sample holder of the PPMS system with the electromagnet poles. The direction of magnetic field is perpendicular to the plane of the sample as described in Fig. 6(b). Figures 8(a) and 8(b) represent the values of magnetoresistance for sample S1 and Figs. 8(c) and 8(d) for sample S2 as a function of magnetic field at different temperatures. Both positive and negative magnetoresistance (MR) are obtained in our sample. Interestingly, it is noted that in the metallic region MR shows positive values; however, in the semiconducting regions at both ends of the metallic phase, negative MR values are obtained. In the regime of weak localization, we have considered electron-electron ( $e$ - $e$ ) interaction [35] for positive and spin-spin scattering [36] as negative contributions of magnetoresistance, respectively. Considering these two terms, the expression for magnetoresistance may be written as

$$\frac{\Delta\rho}{\rho} = aH^{1/2} - b^2 \ln(1 + c^2 H^2). \quad (8)$$

Here, the first term represents the  $e$ - $e$  interaction which gives positive magnetoresistance and the second term represents the scattering of electrons with the localized spins giving rise to negative magnetoresistance. The prefactor  $a$  in the first term is a constant at constant temperature. However, the expressions for  $b$  and  $c^2$  are given by

$$b = A_1 J D_F [S(S+1)\langle\chi^2\rangle], \quad (9)$$

$$c^2 = \left[ 1 + 4S^2 \Pi^2 \left( \frac{2J D_F}{g} \right)^4 \right] \left( \frac{g\mu_B}{\beta k_B T} \right)^2, \quad (10)$$

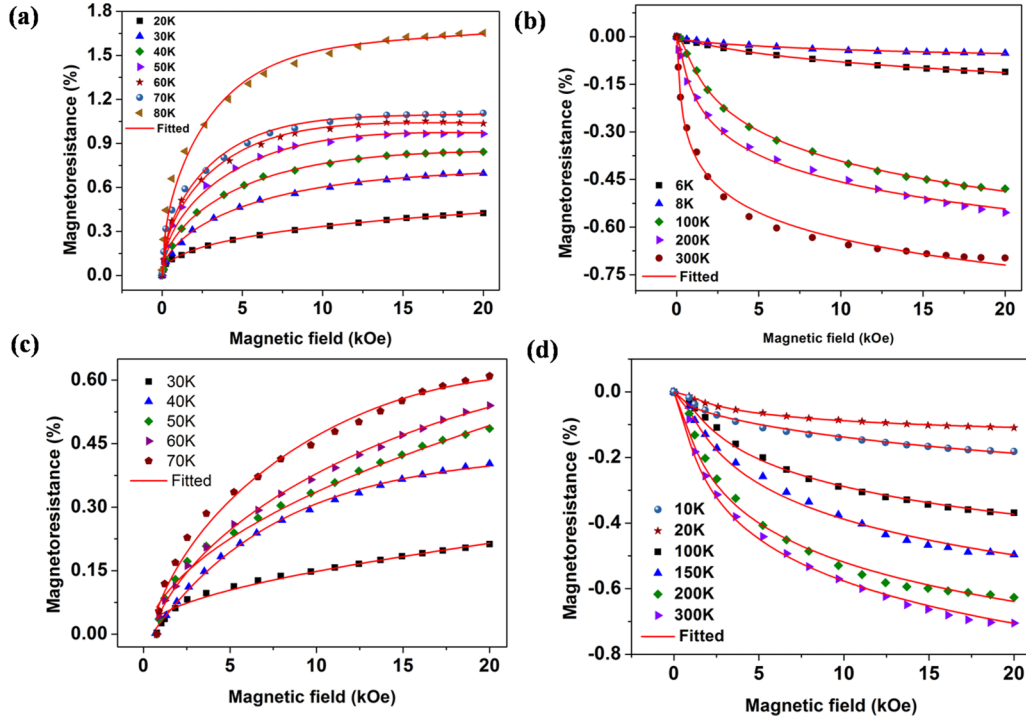


FIG. 8. Magnetoresistance values at different temperatures for sample S1 (a) in the metallic region which is positive and (b) on either side of the metallic region which is negative. For the sample S2, (c) MR in the metallic region and (d) MR on either side of the metallic region.

where  $J$  is the exchange interaction energy,  $g$  is the Landé  $g$  factor,  $D_F$  is the density of states at the Fermi energy,  $\langle \chi \rangle$  is the average magnetization,  $S$  is the spin of the localized magnetic moment, and  $\beta$  is a numerical constant with values ranging from 0.1 to 10.

The magnetoresistance data at a fixed temperature are fitted by Eq. (8) taking  $a$ ,  $b$ , and  $c$  as constants. The solid lines represent the theoretical curves as obtained by Eq. (8), whereas the points are the experimental data. The extracted parameters obtained by the fitting procedure are summarized in Table IV. Interestingly, it appears from both the figures that positive magnetoresistance is obtained only in the metallic region; however, outside the metallic region at both ends

of the high- and low-temperature regions magnetoresistance becomes negative.

Therefore, to explain the complicated MR results we have considered only the  $e-e$  interaction and the scattering of spin-polarized electrons with the localized spins as scattering centers. As mentioned above, the charge transfer effect from Ag to MoS<sub>2</sub> at the interface produces a magnetic moment both in MoS<sub>2</sub> and Ag with opposite spin orientation resulting an antiferromagnetic ordering at the interface [37–40].

The scattering of polarized conduction electrons with the spin scattering centers at a particular temperature as a function of field depends on the magnitude of the net moment arising due to thermal misalignment of antiferromagnetic coupling at

TABLE IV. Parameters obtained by fitting the MR data with Eq. (8).

Temperature (K)	S1			Temperature (K)	S2		
	$a$	$b$	$c$		$a$	$b$	$c$
6	$0.15 \pm 0.0021$	$0.89 \pm 0.025$	$2.895 \pm 0.0256$	10	$0.10 \pm 0.001$	$0.43 \pm 0.10$	$0.81 \pm 0.05$
8	$0.23 \pm 0.0033$	$0.875 \pm 0.0015$	$1.987 \pm 0.0125$	20	$0.13 \pm 0.01$	$0.41 \pm 0.065$	$0.793 \pm 0.03$
20	$0.377 \pm 0.0031$	$0.1625 \pm 0.051$	$0.25 \pm 0.029$	30	$0.14 \pm 0.03$	$0.04 \pm 0.001$	$0.042 \pm 0.02$
30	$0.71 \pm 0.0266$	$0.372 \pm 0.010$	$0.3 \pm 0.006$	40	$0.359 \pm 0.10$	$0.238 \pm 0.02$	$0.133 \pm 0.04$
40	$0.917 \pm 0.0122$	$0.517 \pm 0.026$	$0.35 \pm 0.0321$	50	$0.42 \pm 0.06$	$0.27 \pm 0.054$	$0.16 \pm 0.005$
50	$1.147 \pm 0.0064$	$0.68 \pm 0.023$	$0.4 \pm 0.022$	60	$0.50 \pm 0.05$	$0.32 \pm 0.02$	$0.18 \pm 0.04$
60	$1.357 \pm 0.0166$	$0.64 \pm 0.051$	$0.7 \pm 0.01$	70	$0.56 \pm 0.002$	$0.32 \pm 0.09$	$0.21 \pm 0.09$
70	$1.489 \pm 0.002$	$0.65 \pm 0.03$	$0.9 \pm 0.032$	100	$0.29 \pm 0.01$	$0.44 \pm 0.03$	$0.85 \pm 0.007$
80	$2.136 \pm 0.23$	$0.841 \pm 0.11$	$1.02 \pm 0.09$	150	$0.19 \pm 0.04$	$0.5 \pm 0.10$	$0.91 \pm 0.07$
100	$1.40 \pm 0.19$	$0.90 \pm 0.01$	$3.733 \pm 0.32$	200	$0.112 \pm 0.09$	$0.623 \pm 0.05$	$1.15 \pm 0.35$
200	$0.891 \pm 0.14$	$0.99 \pm 0.12$	$5.696 \pm 0.48$	300	$0.08 \pm 0.003$	$0.68 \pm 0.11$	$1.45 \pm 0.25$
300	$0.764 \pm 0.21$	$1.05 \pm 0.29$	$7.526 \pm 0.64$				

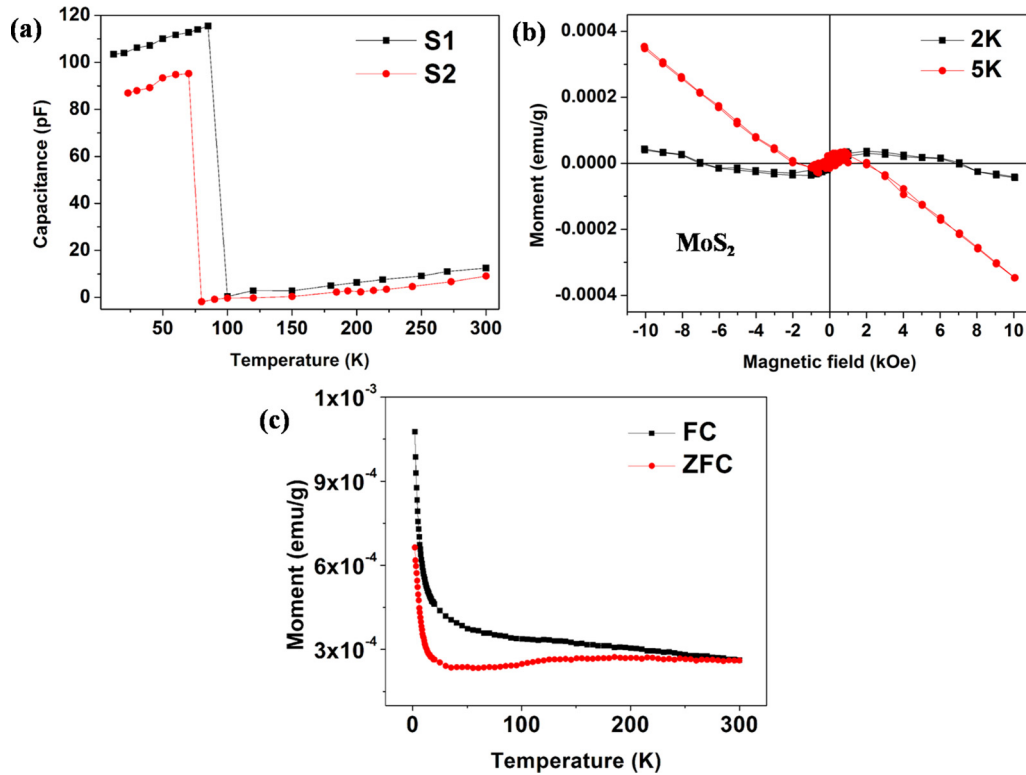


FIG. 9. (a) Capacitance versus temperature plot for samples S1 and S2. (b)  $M$ - $H$  loops of pristine  $\text{MoS}_2$  at 2 and 5 K. (c) ZFC-FC magnetization curve with temperature of a typical composite.

the interface. At the highest temperature (300 K), the magnetic moment generated due to thermal agitation for antiferromagnetic coupling under the magnetic field is the maximum. Therefore, at this temperature the negative magnetoresistance as a function of magnetic field reaches the maximum value. As temperature decreases, the net moment at the interface becomes smaller due to stronger antiferromagnetic coupling at lower temperature resulting in lower magnetoresistance [41]. For S1, this decrease in negative magnetoresistance at lower temperature continues down to 100 K. With further decrease of temperature, a positive magnetoresistance is observed in the temperature range from 20 to 80 K (for S2 from 30 to 70 K) due to the metallic state originated as a result of charge transfer effect at the interface, discussed earlier. The origin of positive magnetoresistance in this temperature range is the strong  $e$ - $e$  interaction in the metallic state [42,43]. It appears that negative MR due to spin scattering effect decreases with decreasing temperature; however, due to  $e$ - $e$  interaction it increases with increasing temperature. Because of these competing effects, the positive MR gives the highest value at 80 K and decreases with decreasing temperature down to 20 K.

At very low temperature below 20 K, a negative MR is again observed due to the spin scattering effect of the polarized electrons with the localized spins at the interface [44–46]. This is because of the fact that the magnetic spins corresponding to holes generated in silver due to charge transfer effect result in stronger ferromagnetic coupling among the spins in the silver atoms. Therefore, the negative magnetoresistance at very low temperature arises due to scattering of spin-polarized electrons with the net spin in silver nanoparticles at the interface. In this

case, the MR feature is different from that obtained at higher temperature. Here the magnitude of negative MR increases with lowering of temperature, as usual in the case of spin scattering systems.

The metallic phase is supported not only by positive magnetoresistance, but also dielectric measurements are carried out over the same temperature range. It is seen that the capacitance value increases near the insulator-to-metal transition [47] as shown in Fig. 9(a).

### C. Magnetization and hysteresis loop

Due to vacancy in  $\text{MoS}_2$ , weak ferromagnetism can come from the  $1T$  phase [48]. We have synthesized  $\text{MoS}_2$  sheets by the same procedure without the presence of Ag nanoparticles and carried out the hysteresis loop as given in Fig. 9(b). From the figure, it is clearly observed that loops are diamagnetic in nature as observed for the  $2H$ - $\text{MoS}_2$  phase. Therefore, the  $1T$  phase is not dominant here as the overall magnetism of the bare  $\text{MoS}_2$  phase is nonmagnetic in nature.

To investigate the temperature-dependent magnetization as a function of magnetic field for all samples, magnetic measurements such as zero-field cooling (ZFC), field cooling (FC), and magnetization as a function of field have been carried out over the temperature range from 2 to 300 K. The ZFC-FC curve and hysteresis loops for samples S1 and S2 are shown in Figs. 9(c) and 10, respectively, which are typical of all samples. A bifurcation in ZFC-FC and the hysteresis loop with coercivity of 232 Oe for sample S1 and 340 Oe for sample S2 at 2 K indicate the weak ferromagnetic ordering at the lower-temperature region. The observed ferromagnetism

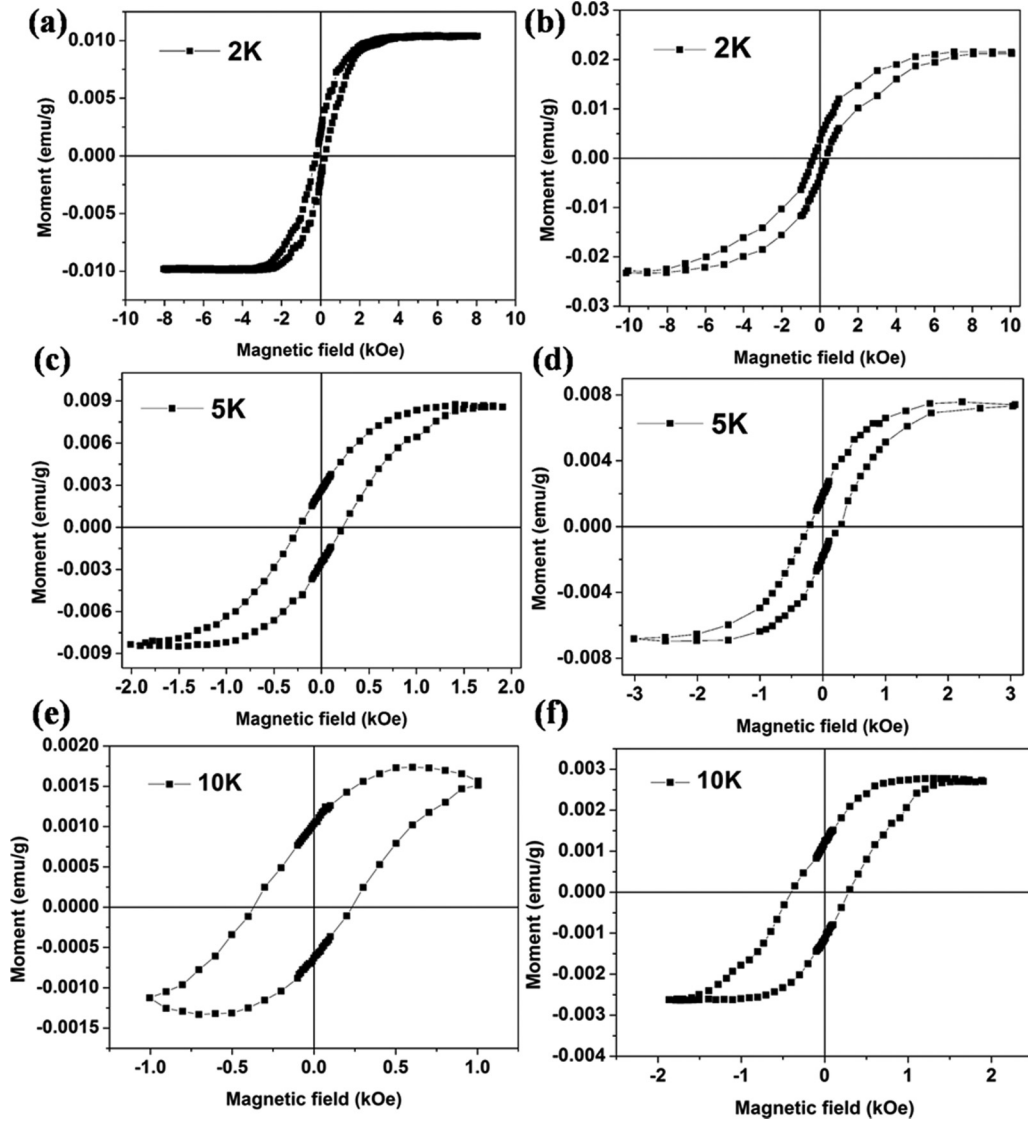


FIG. 10.  $M$ - $H$  loops at 2 K for sample (a) S1, (b) S2; at 5 K for sample (c) S1, (d) S2; and at 10 K for sample (e) S1, (f) S2.

arises due to dominant coupling between the magnetic spins generated due to localized holes [20,21] in silver nanoparticles as a result of charge transfer as discussed in an earlier section (Sec. III B) explaining the MR results. We have measured a hysteresis loop up to a temperature of 10 K after which the sample behaves as if diamagnetic. The hysteresis loop generated due to localized spin ordering originates as a result of charge transfer from Ag to MoS<sub>2</sub>. This is the maximum only at low temperature where uncompensated localized hole spin states in Ag dominate, so it is believed that at higher temperature due to lack of sufficient uncompensated spin states no ferromagnetic loop will be observed.

#### IV. DFT CALCULATION FOR CHARGE TRANSFER PROCESS AND TEMPERATURE EFFECT

##### A. Computational details

The electronic calculations for a MoS<sub>2</sub> layer decorated with silver nanoparticles are performed in the framework of density functional theory using the Vienna *Ab-Initio* Simulation

Package (VASP) [49,50] considering the projector-augmented-wave (PAW) [51] method. For the treatment of exchange-correlation functions, the generalized gradient approximation (GGA) is considered through Perdew-Burke-Ernzerhof (PBE) [52] parametrization. The plane-wave expansion is terminated by setting cutoff energy to 450 eV. The lattice parameters and ionic positions are optimized using the conjugate gradient (CG) method until the Hellmann-Feynman force components are less than 0.001 eV/Å. The self-consistency calculations are performed until the energy variation between two successive iterations is smaller than 10<sup>-5</sup> eV. The reciprocal space is integrated using 7 × 7 × 1  $k$ -point set via the Monkhorst-Pack scheme [53]. The electronic charge transfer is evaluated through the Bader method, an algorithm developed by Henkelman and co-workers [54].

To find out the charge transfer mechanism between the Ag nanoparticle and the MoS<sub>2</sub> layer, we performed the *ab initio* calculations. First, the Ag<sub>13</sub> cluster is optimized by considering a 15 × 15 × 15 Å unit cell separately, and then a 4 × 4 × 1 supercell of the MoS<sub>2</sub> layer with cell dimensions of 12.7 ×

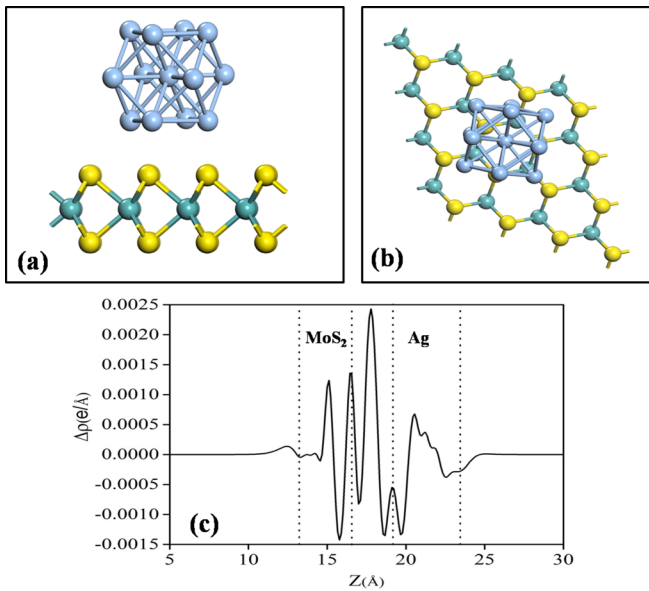


FIG. 11. (a) Side and (b) top view of the model structures Ag<sub>13</sub>/MoS<sub>2</sub> heterostructure. The green, yellow, and blue spheres correspond to Mo, S, and Ag atoms, respectively. (c) Planar average charge density difference for Ag<sub>13</sub>/MoS<sub>2</sub>.

$12.7 \times 20 \text{ \AA}$  is optimized. Then the Ag@MoS<sub>2</sub> (the top of the MoS<sub>2</sub> decorated with an Ag<sub>13</sub> nanocluster) heterostructure is constructed and to avoid the interactions between adjacent images, we considered a vacuum of  $30 \text{ \AA}$  along the  $c$  direction. The Ag@MoS<sub>2</sub> model structure contains a total of 61 atoms

(16 Mo, 32 S, 13 Ag). The optimized configuration of the Ag decorated MoS<sub>2</sub> structure is shown in Figs. 11(a) and 11(b) (side view and top view). The four Ag atoms of the Ag nanocluster are interacting with surface S atoms on the MoS<sub>2</sub> surface, which leads to the formation of the Ag@MoS<sub>2</sub> structure.

### B. Theoretical calculation for charge transfer

Our calculation results clearly show that the interaction between the Ag nanoparticles and MoS<sub>2</sub> sheets involves considerable charge transfer in the associated elements (interaction between Ag atoms and surface S atoms). In order to explore the chemical environment (mainly the charge transfer effect) due to the formation of the Ag@MoS<sub>2</sub> composite, we quantitatively analyzed the planar averaged charge density difference

$$\Delta_{\text{rho}} = \rho_{\text{MoS}_2/\text{Ag}} - \rho_{\text{MoS}_2} - \rho_{\text{Ag}},$$

where  $\rho_{\text{MoS}_2/\text{Ag}}$ ,  $\rho_{\text{MoS}_2}$ , and  $\rho_{\text{Ag}}$  are the charge densities of the Ag nanoparticles over MoS<sub>2</sub>, MoS<sub>2</sub> sheets, and Ag nanoparticles, respectively. The profile of the planar averaged charge density as a function of position in the  $z$  direction is presented in Fig. 11(c). The negative and positive values in the graph correspond to the charge depletion and accumulation, respectively. We observed that the charge accumulation region is covered by the MoS<sub>2</sub> surface region and accumulation occurred mainly on the surface S atom region (dotted vertical line at  $16.6 \text{ \AA}$ ). The complete charge depletion region is observed at the interface of Ag@MoS<sub>2</sub> (dotted vertical line at  $19.2 \text{ \AA}$ ). From this study, we can conclude that the charge has transferred from Ag atoms (which are interacting directly with

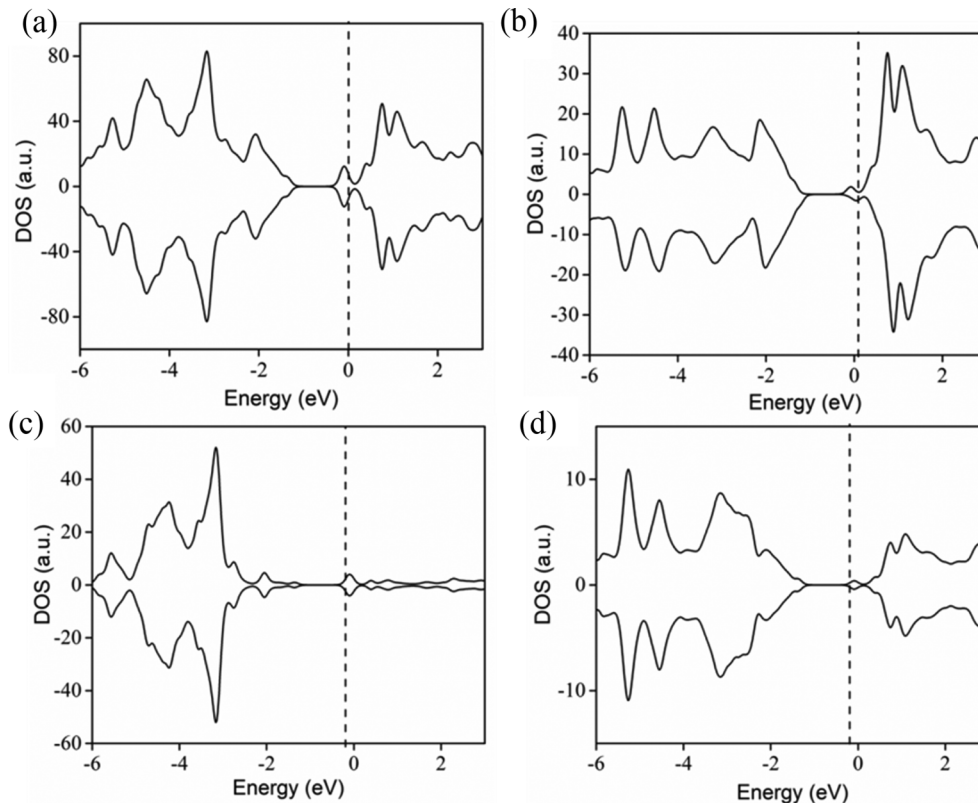


FIG. 12. Total density of states (TDOS) and partial density of states (PDOS) of (a) Ag<sub>13</sub>/MoS<sub>2</sub>, (b) MoS<sub>2</sub>, (c) Ag<sub>13</sub>, and (d) S atom.

TABLE V. Integral value of valence electron of single Ag atom interaction with the MoS<sub>2</sub> layer at different temperature values considered in molecular dynamics (MD) simulation.

Temperature (K)	$\int_{-\infty}^0 \rho_{\text{val}} dE$
0	7.43
20	9.21
50	10.86
100	11.00
150	11.00
250	11.10
300	11.10

surface S atoms) to S atoms in the MoS<sub>2</sub> layer. To confirm the above analysis, we performed the Bader charge analysis to extract the quantitative result. The net positive charge on the Ag cluster (+0.038 *e*) directly indicates that the charge is transferred from the Ag atom to the MoS<sub>2</sub> surface.

### C. DOS calculation

For deeper insight we studied the density of states (DOS) analysis of the Ag<sub>13</sub>@MoS<sub>2</sub> nanostructure. The DOSs of the heterostructures are shown in Fig. 12(a). The partial DOS of the MoS<sub>2</sub> layer and the Ag<sub>13</sub> nanocluster is shown in Figs. 12(b) and 12(c). The partial DOS of the S atoms of the MoS<sub>2</sub> layer is demonstrated in Fig. 12(d). From Fig. 12 it can be easily revealed that a shallow donor level is created near the Fermi energy due to surface doping. The donor level is created mainly due to the charge transfer and hybridization between the Ag<sub>13</sub> nanoparticle and the MoS<sub>2</sub> layer. The semiconductor characteristic of MoS<sub>2</sub> is retained even after surface doping.

### D. Temperature effect

To check the effect of temperature on the charge transfer mechanism we did *ab initio* based molecular dynamics simulations. The temperature range 0, 20, 50, 100, 150, 250, and 300 K has been used considering the Nosé thermostat within the *NVT* ensemble [55]. For the equilibration, we used 1000 time steps with each step 1 fs long.

We consider the structure at the given temperature to calculate the occupancy and the charge redistribution of the

valence electron of a single Ag atom interacting with the MoS<sub>2</sub> layer; it is shown in Table V. From Table V, the integral value of the valence electron is slightly changed at higher temperature, but in the low-temperature range a considerable amount of change is observed indicating better charge transfer rate at low temperature. In the high-temperature region, charge transfer does not occur much due to an activated process but in the low-temperature range a better charge transfer rate is observed due to strong coupling among the orbitals of Ag and MoS<sub>2</sub>. Similar projection of the orbital to find the electron occupancy is done in a few other works in the literature [56,57]. From Table V, the amount of charge transfer obtained here is of the same order as that obtained in other reports [20,58]. Thus, in the low-temperature region the decrease in the valence electron of Ag indicates better charge transfer effect at low temperature.

## V. CONCLUSION

In conclusion, MoS<sub>2</sub> sheets are decorated by Ag nanoparticles to investigate interesting ferromagnetic ordering, charge transport, and magnetotransport as arising due to charge transfer between Ag and MoS<sub>2</sub>. It is seen that the charge transfer from Ag to MoS<sub>2</sub> modifies significantly to develop ferromagnetic ordering at the low-temperature region, the metal-insulator transition resulting from positive to negative magnetoresistance. Dominant magnetic coupling among the spins of localized holes in Ag nanoparticles at lower temperature over the interfacial antiferromagnetic coupling and additional localized states due to charge transfer in MoS<sub>2</sub> are the origin of the observed ferromagnetism and M-I transition. Theoretical calculation is done to verify the charge transfer process and the temperature effect. This kind of study will be helpful for controlling magnetism at the nanoscale on substrates with many functionalities.

## ACKNOWLEDGMENTS

S. Bag, S. Bhattacharya, and D.D. acknowledge the Department of Science and Technology (DST)-INSPIRE, Council of Scientific & Industrial Research (CSIR)-SPM, and CSIR, New Delhi, respectively, for awarding their fellowships. S.K.S. acknowledges DST, New Delhi, Government of India, for the infrastructural facility.

- 
- [1] K. S. Novoselov, A. K. Geim, S. V. Morozov, D. Jiang, M. I. Katsnelson, I. V. Grigorieva, S. V. Dubonos, and A. A. Firsov, *Nature* **438**, 197 (2005).
- [2] K. S. Novoselov, Z. Jiang, Y. Zhang, S. V. Morozov, H. L. Stormer, U. Zeitler, J. C. Maan, G. S. Boebinger, P. Kim, and A. K. Geim, *Science* **315**, 1379 (2007); P. Hota, A. J. Akhtar, S. Bhattacharya, M. Miah, and S. K. Saha, *Appl. Phys. Lett.* **111**, 042402 (2017).
- [3] P. Blake, P. D. Brimicombe, R. R. Nair, T. J. Booth, D. Jiang, F. Schedin, L. A. Ponomarenko, S. V. Morozov, H. F. Gleeson, E. W. Hill, A. K. Geim, and K. S. Novoselov, *Nano Lett.* **8**, 1704 (2008).
- [4] S. K. Saha, M. Baskey, and D. Majumdar, *Adv. Mater.* **22**, 5531 (2010).
- [5] S. Bhattacharya, E. M. Kumar, R. Thapa, and S. K. Saha, *Appl. Phys. Lett.* **110**, 032404 (2017).
- [6] W. Park, J. Baik, T.-Y. Kim, K. Cho, W.-K. Hong, H.-J. Shin, and T. Lee, *ACS Nano* **8**, 4961 (2014).
- [7] Q. H. Wang, K. Kalantar-Zadeh, A. Kis, J. N. Coleman, and M. S. Strano, *Nat. Nanotechnol.* **7**, 699 (2012).
- [8] F. Bonaccorso, Z. Sun, T. Hasan, and A. C. Ferrari, *Nat. Photonics* **4**, 611 (2010).
- [9] J. Klinovaja and D. Loss, *Phys. Rev. B* **88**, 075404 (2013).
- [10] S. Bhattacharya and S. K. Saha, *Macromol. Symp.* **376**, 1600183 (2017).
- [11] D. Higgins, P. Zamani, A. Yu, and Z. Chen, *Energy Environ. Sci.* **9**, 357 (2016).

- [12] F. Z. Wang, M. J. Zheng, B. Zhang, C. Q. Zhu, Q. Li, L. Ma, and W. Z. Shen, *Sci. Rep.* **6**, 31092 (2016).
- [13] A. K. Mishra, K. V. Lakshmi, and L. Huang, *Sci. Rep.* **5**, 15718 (2015).
- [14] D. Dinda, M. E. Ahmed, S. Mandal, B. Mondal, and S. K. Saha, *J. Mater. Chem. A* **4**, 15486 (2016).
- [15] Y. Wang, S. Li, and J. Yi, *Sci. Rep.* **6**, 24153 (2016).
- [16] A. Ramasubramaniam and D. Naveh, *Phys. Rev. B* **87**, 195201 (2013).
- [17] R. Mishra, W. Zhou, S. J. Pennycook, S. T. Pantelides, and J. C. Idrobo, *Phys. Rev. B* **88**, 144409 (2013).
- [18] S. Bhattacharya, D. Dinda, B. K. Shaw, S. Dutta, and S. K. Saha, *Phys. Rev. B* **93**, 184403 (2016).
- [19] D. Sarkar, X. Xie, J. Kang, H. Zhang, W. Liu, J. Navarrete, M. Moskovits, and K. Banerjee, *Nano Lett.* **15**, 2852 (2015).
- [20] P. Crespo, R. Litrán, T. C. Rojas, M. Multigner, J. M. de la Fuente, J. C. Sánchez-López, M. A. García, A. Hernando, S. Penadés, and A. Fernández, *Phys. Rev. Lett.* **93**, 087204 (2004).
- [21] L. Suber, D. Fiorani, G. Scavia, and P. Imperatori, *Chem. Mater.* **19**, 1509 (2007).
- [22] G. L. Nealon, B. Donnio, R. Greget, J. P. Kappler, E. Terazzib, and J. L. Gallani, *Nanoscale* **4**, 5244 (2012).
- [23] G. K. Wertheim, S. B. DiCenzo, and S. E. Youngquist, *Phys. Rev. Lett.* **51**, 2310 (1983).
- [24] M. G. Mason, *Phys. Rev. B* **27**, 748 (1983).
- [25] P. Torelli, L. Giordano, S. Benedetti, P. Luches, E. Annese, S. Valeri, and G. Pacchioni, *J. Phys. Chem. C* **113**, 19957 (2009).
- [26] A. K. Das, P. Misra, R. S. Ajimsha, A. Bose, S. C. Joshi, D. M. Phase, and L. M. Kukreja, *J. Appl. Phys.* **112**, 103706 (2012).
- [27] N. Sclar, *Phys. Rev.* **104**, 1559 (1956).
- [28] E. E. Mendez, P. J. Price, and M. Heiblum, *Appl. Phys. Lett.* **45**, 294 (1984).
- [29] T. A. Skotheim, R. L. Elsenbaumer, and J. R. Reynolds, *Handbook of Conducting Polymers* (CRC Press, Boca Raton, FL, 2007), p. 35.
- [30] R. Fivaz and E. Mooser, *Phys. Rev.* **163**, 743 (1967).
- [31] R. Ganatra and Q. Zhang, *ACS Nano* **8**, 4074 (2014).
- [32] L. M. S. Alves, V. I. Damasceno, C. A. M. dos Santos, A. D. Bortolozzo, P. A. Suzuki, H. J. Izario Filho, A. J. S. Machado, and Z. Fisk, *Phys. Rev. B* **81**, 174532 (2010).
- [33] S. Mandal, A. J. Akhtar, B. K. Shaw, and S. K. Saha, *Phys. Status Solidi RRL* **9**, 544 (2015).
- [34] M. Rütten, M. Kaes, A. Albert, M. Wuttig, and M. Salinga, *Sci. Rep.* **5**, 17362 (2015).
- [35] T. A. Skotheim, R. L. Elsenbaumer, and J. R. Reynolds, *Handbook of Conducting Polymers* (CRC Press, Boca Raton, FL, 2007), p. 41.
- [36] R. P. Khosla and J. R. Fischer, *Phys. Rev. B* **2**, 4084 (1970).
- [37] A. J. Akhtar, A. Gupta, D. Chakravorty, and S. K. Saha, *AIP Adv.* **3**, 072124 (2013).
- [38] P. Wu, N. Yin, P. Li, W. Chenga, and M. Huang, *Phys. Chem. Chem. Phys.* **19**, 20713 (2017).
- [39] S. Mandal and S. K. Saha, *J. Appl. Phys.* **117**, 093910 (2015).
- [40] H. Shu, P. Luo, P. Liang, D. Cao, and X. Chen, *ACS Appl. Mater. Interfaces* **7**, 7534 (2015).
- [41] M. N. Baibich, J. M. Broto, A. Fert, F. Nguyen Van Dau, F. Petroff, P. Etienne, G. Creuzet, A. Friederich, and J. Chazelas, *Phys. Rev. Lett.* **61**, 2472 (1988).
- [42] A. Gerber, I. Kishon, I. Y. Korenblit, O. Riss, A. Segal, M. Karpovski, and B. Raquet, *Phys. Rev. Lett.* **99**, 027201 (2007).
- [43] A. B. Pippard, *Magnetoresistance in Metals* (Cambridge University Press, Cambridge, 1989).
- [44] S. Mandal and S. K. Saha, *Nanoscale* **4**, 986 (2012).
- [45] D. Sun, L. Yin, C. Sun, H. Guo, Z. Gai, X.-G. Zhang, T. Z. Ward, Z. Cheng, and J. Shen, *Phys. Rev. Lett.* **104**, 236602 (2010).
- [46] C. Bellouard, H. D. Rapp, B. George, S. Mangin, G. Marchal, and J. C. Ousset, *Phys. Rev. B* **53**, 5082 (1996).
- [47] P. K. Mukherjee, K. Chatterjee, and D. Chakravorty, *Phys. Rev. B* **73**, 035414 (2006).
- [48] L. Cai, J. He, Q. Liu, T. Yao, L. Chen, W. Yan, F. Hu, Y. Jiang, Y. Zhao, T. Hu, Z. Sun, and S. Wei, *J. Am. Chem. Soc.* **137**, 2622 (2015).
- [49] G. Kresse and J. Furthmüller, *Phys. Rev. B* **54**, 11169 (1996).
- [50] G. Kresse and J. Hafner, *Phys. Rev. B* **48**, 13115 (1993).
- [51] G. Kresse and D. Joubert, *Phys. Rev. B* **59**, 1758 (1999).
- [52] J. P. Perdew, K. Burke, and M. Ernzerhof, *Phys. Rev. Lett.* **77**, 3865 (1996).
- [53] H. J. Monkhorst and J. D. Pack, *Phys. Rev. B* **13**, 5188 (1976).
- [54] W. Tang, E. Sanville, and G. Henkelman, *J. Phys: Condens. Matter* **21**, 084204 (2009).
- [55] S. Nosé, *J. Chem. Phys.* **81**, 511 (1984).
- [56] S. Sinthika, U. V. Waghmare, and R. Thapa, *Small* **14**, 1703609 (2017).
- [57] A. Rajkamal, S. Sinthika, G. Andersson, and R. Thapa, *Carbon* **129**, 775 (2018).
- [58] P. Zhang and T. K. Sham, *Appl. Phys. Lett.* **81**, 736 (2002).